

1 Quantifying the impact of aerosol scattering on the 2 retrieval of methane from airborne remote sensing 3 measurements

4
5 Yunxia Huang^{1,2}, Vijay Natraj³, Zhaocheng Zeng^{2,4}, Pushkar Kopparla⁵, and Yuk L.
6 Yung^{2,3}

7
8 ¹School of Science, Nantong University, Nantong, 226007, China

9 ²Division of Geological and Planetary Sciences, California Institute of Technology, Pasadena, CA 91125,
10 USA

11 ³Jet Propulsion Laboratory, California Institute of Technology, Pasadena, CA 91109, USA

12 ⁴Joint Institute for Regional Earth System Science and Engineering, University of California, Los
13 Angeles, CA 90095, USA

14 ⁵Graduate School of Frontier Sciences, The University of Tokyo, Kashiwa, Chiba 277-0882, Japan

15
16 *Correspondence to:* Vijay Natraj (vijay.natraj@jpl.nasa.gov)

17
18 **Abstract.** As a greenhouse gas with strong global warming potential, atmospheric methane (CH₄)
19 emissions have attracted a great deal of attention. Although remote sensing measurements can provide
20 information about CH₄ sources and emissions, accurate retrieval is challenging due to the influence of
21 atmospheric aerosol scattering. In this study, imaging spectroscopic measurements from the Airborne
22 Visible/Infrared Imaging Spectrometer–Next Generation (AVIRIS-NG) in the short-wave infrared are
23 used to compare two retrieval techniques — the traditional Matched Filter (MF) method and the Optimal
24 Estimation (OE) method, which is a popular approach for trace gas retrievals. Using a numerically
25 efficient two-stream-exact-single-scattering radiative transfer model, we also simulate AVIRIS-NG
26 measurements for different scenarios and quantify the impact of aerosol scattering in the two retrieval
27 schemes by including aerosols in the simulations but not in the retrievals. The presence of aerosols causes
28 an underestimation of CH₄ in both the MF and OE retrievals; the biases increase with increasing surface
29 albedo and aerosol optical depth (AOD). Aerosol types with high single scattering albedo and low
30 asymmetry parameter (such as water soluble aerosols) induce large biases in the retrieval. When
31 scattering effects are neglected, the MF method exhibits lower fractional retrieval bias compared to the
32 OE method at high CH₄ concentrations (2–5 times typical background values), and is suitable for
33 detecting strong CH₄ emissions. For an AOD value of 0.3, the fractional biases of the MF retrievals are

34 between 1.3 and 4.5%, while the corresponding values for OE retrievals are in the 2.8–5.6% range. On
35 the other hand, the OE method is an optimal technique for diffuse sources (<1.5 times typical background
36 values), showing up to five times smaller fractional retrieval bias (8.6%) than the MF method (42.6%)
37 for the same AOD scenario. However, when aerosol scattering is significant, the OE method is superior
38 since it provides a means to reduce biases by simultaneously retrieving AOD, surface albedo and CH₄.
39 The results indicate that, while the MF method is good for plume detection, the OE method should be
40 employed to quantify CH₄ concentrations, especially in the presence of aerosol scattering.

41 **1 Introduction**

42 Atmospheric methane (CH₄) is about 85 times more potent per unit mass at warming the Earth than
43 carbon dioxide (CO₂) on a 20-year timescale (IPCC, 2013), implying that reduction in CH₄ emissions
44 could be very efficient to slow down global warming in the near term. Global mean CH₄ concentrations
45 have increased from ~700 ppb in the preindustrial era to more than 1860 ppb as of 2019 (NOAA, 2019).
46 The most effective sink of atmospheric CH₄ is the hydroxyl radical (OH) in the troposphere. CH₄ reacts
47 with OH to reduce the oxidizing capacity of the atmosphere and generate tropospheric ozone. Increasing
48 emissions of CH₄ reduce the concentration of OH in the atmosphere. With less OH to react with, the
49 lifespan of CH₄ could also increase, resulting in greater CH₄ concentrations (Holmes et al., 2013). Soils
50 also act as a major sink for atmospheric methane through the methanotrophic bacteria that reside within
51 them.

52 Significant natural CH₄ sources include wetlands (Bubier et al., 1994, Macdonald et al., 1998;
53 Gedney et al., 2004), geological seeps (Kvenvolden and Rogers, 2005; Etiope et al., 2009), ruminant
54 animals, and termites. In addition, increased surface and ocean temperatures associated with global
55 warming may increase CH₄ emissions from melting permafrost (Woodwell et al., 1998; Walter et al.,
56 2006; Schaefer et al., 2014, Schuur et al., 2015) and methane hydrate destabilization (Kvenvolden, 1988;
57 Archer, 2007). Human activity also contributes significantly to the total CH₄ emissions. Rice agriculture
58 is one of the most important anthropogenic sources of CH₄ (Herrero et al., 2016; Schaefer et al., 2016).
59 Other sources include landfills (Themelis and Ulloa, 2007), wastewater treatment, biomass burning, and
60 methane slip from gas engines. Global fugitive CH₄ emissions from coal mining (Kort et al., 2014),
61 natural gas and oil systems (Alvarez et al., 2018), hydraulic fracturing (“fracking”) of shale gas wells
62 (Howarth et al., 2011; Howarth, 2015, 2019), and residential and commercial natural gas distribution
63 sectors (He et al., 2019) are also of increasing concern. Although the sources and sinks of methane are
64 reasonably well known, there are large uncertainties in their relative amounts and in the partitioning
65 between natural and anthropogenic contributions (Nisbet et al., 2014, 2016). This uncertainty is
66 exemplified by the CH₄ “hiatus”, which refers to the observed stabilization of atmospheric CH₄
67 concentrations from 1999–2006, and the renewed rise thereafter (Kirschke et al., 2013).

68 Satellite monitoring of CH₄ can be broadly divided into three categories: solar backscatter, thermal
69 emission and lidar (Jacob et al., 2016). The first solar backscattering mission was SCIAMACHY
70 (Frankenberg et al., 2006), which was operational from 2003–2012 and observed the entire planet once
71 every seven days. It was followed by GOSAT in 2009 (Kuze et al., 2016), and subsequently the next
72 generation GOSAT-2 in 2018 (Glumb et al., 2014). In between, the TROPOMI mission was also
73 launched in 2017, which observes the planet once daily with a high spatial resolution of 7×7 km² (Butz

74 et al., 2012; Veeffkind et al., 2012). CarbonSat (Buchwitz et al., 2013) is another proposed mission to
75 measure CH₄ globally from solar backscatter with a very fine spatial resolution (2×2 km²) and high
76 precision (0.4%). GHGSat-D (McKeever et al., 2017; Varon et al., 2019; Jervis et al., 2020) measures
77 between 1630–1675 nm, with an effective pixel resolution of 50×50 m² over targeted 12×12 km² scenes,
78 and is intended to detect CH₄ emissions from individual industrial sites. In contrast, MethaneSAT (Wofsy
79 and Hamburg, 2019) has a pixel size of 1–2 km² and a wide field of view (200 km²) and can quantify
80 diffuse CH₄ emission sources over large areas. Thermal infrared observations of CH₄ are available from
81 the IMG (Clerbaux et al., 2003), AIRS (Xiong et al., 2008), TES (Worden et al., 2012), IASI (Xiong et
82 al., 2013), and CrIS (Gambacorta et al., 2016) instruments. These instruments provide day/night
83 measurements at spatial resolutions ranging from 5×8 km² (TES) to 45×45 km² (AIRS). GEO-CAPE
84 (Fishman et al., 2012), GeoFTS (Xi et al., 2015), G3E (Butz et al., 2015), and GeoCarb (Polonsky et al.,
85 2014) are proposed geostationary instruments (GeoCarb was selected by NASA under the Earth Venture
86 - Mission program), which when operational will have resolutions of 2–5 km over regional scales. The
87 MERLIN lidar instrument (Kiemle et al., 2014) scheduled for launch in 2021 will measure CH₄ by
88 employing a differential absorption lidar.

89 By combining a large number of footprints and high spatial resolution, airborne imaging
90 spectrometers are also well suited for mapping local CH₄ plumes. The Airborne Visible/Infrared Imaging
91 Spectrometer–Next Generation (AVIRIS-NG) measures reflected solar radiance across more than 400
92 channels between 380 and 2500 nm (Green et al., 1998; Thompson et al., 2015). Strong CH₄ absorption
93 features present between 2100 and 2500 nm can be observed at a spectral resolution of 5 nm full width
94 at half maximum (FWHM). A number of approaches have been developed to retrieve CH₄ from such
95 hyperspectral data. Roberts et al. (2010) used a spectral residual approach between 2000 and 2500 nm
96 and Bradley et al. (2011) employed a band ratio technique using the 2298 nm CH₄ absorption band and
97 2058 nm CO₂ absorption band. However, these techniques are not suited for terrestrial locations that
98 have lower albedos and have spectral structure in the SWIR. A cluster-tuned matched filter technique
99 was demonstrated to be capable of mapping CH₄ plumes from marine and terrestrial sources (Thorpe et
100 al., 2013) as well as CO₂ from power plants (Dennison et al., 2013); however, this method does not
101 directly quantify gas concentrations. Frankenberg et al. (2005) developed an iterative maximum *a*
102 *posteriori* differential optical absorption spectroscopy (IMAP-DOAS) algorithm that allows for
103 uncertainty estimation. Thorpe et al. (2014) adapted the IMAP-DOAS algorithm for gas detection in
104 AVIRIS imagery. In addition, they developed a hybrid approach using singular value decomposition and
105 IMAP-DOAS as a complementary method of quantifying gas concentrations within complex AVIRIS
106 scenes.

107 Accurate assessment of CH₄ emissions is particularly challenging in the presence of aerosols
 108 because the latter introduce uncertainties in the light path if not accounted for. In fact, CH₄ emissions are
 109 frequently correlated with pollution due to concurrent aerosol emissions. For large aerosols (such as dust),
 110 the low Ångström exponent values result in high aerosol optical depth (AOD) values even in the
 111 wavelength range from 2000 nm to 2500 nm (Seinfeld and Pandis, 2006; Zhang et al., 2015). Therefore,
 112 it is important to obtain a clear understanding of aerosol impacts on CH₄ retrievals. In this study, SWIR
 113 AVIRIS-NG measurements are used to analyze the impact of aerosol scattering on CH₄ retrievals.
 114 Further, using an accurate but numerically efficient radiative transfer (RT) model (Spurr and Natraj,
 115 2011), we simulate AVIRIS-NG measurements with varying aerosol amounts and quantify the impact of
 116 aerosol scattering using two retrieval techniques, the traditional matched filter (MF) method and the
 117 optimal estimation (OE) method that is widely used in trace gas remote sensing. This article is organized
 118 as follows. The MF and OE retrieval methods are described in Section 2. Section 3 focuses on analysis
 119 of a sample CH₄ plume detected by AVIRIS-NG measurements and compares retrievals using the MF
 120 and OE methods. Section 4 presents a detailed evaluation of aerosol impacts on the two retrieval methods
 121 through simulations of AVIRIS-NG spectra for different geophysical parameters. Section 5 provides a
 122 summary of the work and discusses future research.

123

124 **2 Methods**

125 **2.1 MF method**

126 Real-time remote detection using AVIRIS-NG measurements are traditionally based on the MF
 127 method (Frankenberg et al., 2016). In this method, the background spectra are assumed to be distributed
 128 as a multivariate Gaussian \mathcal{N} with covariance matrix Σ and background mean radiance μ . If H_0 is a
 129 scenario without CH₄ enhancement and H_1 is one with CH₄ enhancement, the MF approach is equivalent
 130 to a hypothesis test between the two scenarios:

$$131 \quad H_0: L_m \sim \mathcal{N}(\mu, \Sigma) \quad (1)$$

$$132 \quad H_1: L_m \sim \mathcal{N}(\mu + t\alpha, \Sigma) \quad (2)$$

133 where L_m is the measurement radiance; t is the target signature, which is defined in Equation (4); α is the
 134 enhancement value, denoting a scaling factor for the target signature that perturbs the background μ . If
 135 x is a vector of measurement spectra with one element per wavelength, $\alpha(x)$ can be written, based on
 136 maximum likelihood estimates (Manolakis et al., 2014), as follows:

$$137 \quad \alpha(x) = \frac{(x - \mu)^T \Sigma^{-1} t}{t^T \Sigma^{-1} t} \quad (3)$$

138 We utilize the same definitions as in Frankenberg et al. (2016). Specifically, the enhancement value $\alpha(\mathbf{x})$
 139 denotes the thickness and concentration within a volume of equivalent absorption, and has units of ppm
 140 \times m. The target signature \mathbf{t} refers to the derivative of the change in measured radiance with respect to a
 141 change in absorption path length due to an optically thin absorbing layer of CH₄. Note that this definition
 142 has the disadvantage that the accuracy of the result degrades when the absorption is strong and further
 143 attenuation becomes nonlinear. At a particular wavelength λ , \mathbf{t} can be expressed as:

$$144 \quad \mathbf{t}(\lambda) = -\kappa(\lambda)\boldsymbol{\mu}(\lambda), \quad (4)$$

145 where κ is the absorption coefficient for a near-surface plume with units of ppm⁻¹ m⁻¹. This is
 146 different from the units of m² · mol⁻¹ traditionally used for the absorption coefficient κ_{trad} in trace
 147 gas remote sensing. Using the ideal gas law to express the volume V (in liters) occupied by one mole of
 148 CH₄ at the temperature and pressure corresponding to the plume altitude ($V = 22.4$ at standard
 149 temperature and pressure), and the relations 1 liter = 10⁻³ m³ and 1 ppm = 10⁻⁶, we obtain the
 150 following expression for unit conversion (units in parentheses):

$$151 \quad \kappa_{trad} [\text{m}^2 \cdot \text{mol}^{-1}] = \kappa [\text{ppm}^{-1} \text{m}^{-1}] \times V [\text{liter mol}^{-1}] \times 10^{-3} [\text{m}^3 \text{liter}^{-1}] / 10^{-6} [\text{ppm}^{-1}] (5)$$

152 Figure 1 shows the target signature, which is calculated based on HITRAN absorption cross-sections
 153 (Rothman et al., 2009). The background mean radiance $\boldsymbol{\mu}$ used in Equation 4 is based on the AVIRIS-
 154 NG measurement shown in Figure 2; this is described in more detail in Section 3.

155 2.2 OE method

156 The OE method is widely used for the remote sensing retrieval of satellite measurements, such as
 157 from the Orbiting Carbon Observatory-2 (OCO-2; O'Dell et al., 2018), the Spinning Enhanced Visible
 158 and Infra-Red Imager (SEVIRI; Merchant et al., 2013), and the Greenhouse Gases Observing Satellite
 159 (GOSAT; Yoshida et al., 2013). It combines an explicit (typically nonlinear) forward model of the
 160 atmospheric state, a (typically Gaussian) prior probability distribution for the variabilities and a (typically
 161 Gaussian) distribution for the spectral measurement errors. In addition, the Bayesian framework used by
 162 the OE approach allows new information (from measurements) to be combined with existing information
 163 (e.g., from models). In many applications, the forward model is nonlinear, and obtaining the optimal
 164 solution requires iterative techniques such as the Levenberg–Marquardt method (Rodgers, 2000), which
 165 has been routinely applied to study the impacts of measurement parameters on the retrieval process (see,
 166 e.g., Zhang et al., 2015). The iteration in this algorithm follows the below procedure.

$$167 \quad \mathbf{x}_{i+1} = \mathbf{x}_i + [(1 + \gamma)\mathbf{S}_a^{-1} + \mathbf{K}_i^T \mathbf{S}_\epsilon^{-1} \mathbf{K}_i]^{-1} \{ \mathbf{K}_i^T \mathbf{S}_\epsilon^{-1} [\mathbf{y} - \mathbf{F}(\mathbf{x}_i)] - \mathbf{S}_a^{-1} [\mathbf{x}_i - \mathbf{x}_a] \} \quad (6)$$

168 where \mathbf{x} is a state vector of surface and atmospheric properties, \mathbf{S}_a is the *a priori* covariance matrix, \mathbf{S}_ϵ
 169 is the spectral radiance noise covariance matrix, \mathbf{K} is the Jacobian matrix, \mathbf{x}_a is the *a priori* state vector
 170 and γ is a parameter determining the size of each iteration step. The measured spectral radiance is denoted

171 as \mathbf{y} ; $\mathbf{F}(\mathbf{x})$ is the simulated radiance obtained from the forward model. For the retrieval of CH_4 from
172 AVIRIS-NG measurements, the state vector includes the total column amounts of CH_4 and H_2O , while
173 for the retrievals from synthetic spectra, the H_2O concentration is fixed and the state vector only includes
174 the CH_4 total column. The *a priori* values are within 10% of the true values; *a priori* errors are assumed
175 to be 20% for all state vector elements. The retrieved results are shown as the column averaged mixing
176 ratio (X_{CH_4} , in ppm). Aerosols are not included in the state vector for both the real and synthetic
177 retrievals. They are, however, considered in the forward model for the synthetic simulations. Table 1
178 (WCRP, 1986) lists optical properties for four basic aerosol types (dust, water soluble, oceanic and soot).
179 Table 2 (WCRP, 1986) shows the corresponding properties for three aerosol models that are defined as
180 mixtures of the basic components from Table 1. We employ the Henyey-Greenstein phase function
181 (Henyey and Greenstein, 1941), where aerosol composition is determined by two parameters: single
182 scattering albedo (SSA) and asymmetry parameter (g). The surface albedo is also not retrieved; for both
183 real and synthetic retrievals, it is held fixed and assumed to be independent of wavelength.

184

185 **3 Detection and retrieval of CH_4 from AVIRIS-NG measurements**

186 To illustrate the OE retrieval and its difference from the MF method, we perform retrievals for an
187 AVIRIS-NG measurement made on 4 September 2014 (ang20140904t204546) in Bakersfield, CA, as
188 shown in Figure 2. The location is to the west of the Kern Front Oil field. This detection is a case study
189 from the NASA/ESA CO_2 and MEthane eXperiment (COMEX) campaign in California during June and
190 August/September 2014, which includes airborne *in situ*, airborne non-imaging remote sensing, and
191 ground-based *in situ* instruments to provide a real-time remote detection and measurement for CH_4
192 plumes released from anthropogenic sources. An RGB image of flight data is displayed in Figure 2a; the
193 emission source is a pump jack, as described in Thompson et al. (2015). Figure 2b presents results from
194 the MF method, which shows that the CH_4 plume disperses downwind and has a maximum enhancement
195 value of about $2800 \text{ ppm} \times \text{m}$. Some artifacts caused by surfaces with strong absorption in the 2100–
196 2500 nm wavelength range, such as oil-based paints or roofs with calcite as a component (Thorpe et al.,
197 2013), also produce large α values in the MF method; these can be removed by an optimization method
198 such as the column-wise MF technique (Thompson et al., 2015).

199 Figure 3 displays the measured radiance (a) before normalization and (b) after normalization,
200 corresponding to two detector elements (in plume and out of plume). Every element is a cross-track
201 spatial location. The normalization is done by calculating the ratio of the radiance to the maximum value
202 across the spectral range, such that the values fall between 0 and 1. This is a first order correction for the
203 effects of surface albedo. Comparing the measured spectrum in plume to that out of plume, there is

204 obvious enhancement of CH₄ that is particularly evident in the normalized radiance. CH₄ is the main
205 absorber in the 2100–2500 nm wavelength range, and H₂O is the major interfering gas. Figure 3b
206 indicates the absorption peaks due to H₂O and CH₄.

207 We choose the plume center with 500 elements to illustrate results obtained using the MF and OE
208 methods. The former evaluates the CH₄ α value compared to the background CH₄ concentration, while
209 the latter retrieves XCH₄. In the MF method, the background covariance matrix Σ and mean radiance
210 μ are drawn from a reference region close to the CH₄ emission source. These are shown in Figure 2,
211 where the dashed green box denotes the reference region and the source is located within the solid red
212 box. In the OE method, results are shown as a multiplicative scaling factor compared to a typical XCH₄
213 background of 1.822 ppm. This value is the globally averaged marine surface annual mean for 2014 (Ed
214 Dlugokencky, NOAA/GML, www.esrl.noaa.gov/gmd/ccgg/trends_ch4/), the year corresponding to the
215 AVIRIS-NG measurement being studied. We use an accurate and numerically efficient two-stream-
216 exact-single-scattering (2S-ESS) RT model (Spurr and Natraj, 2011). This forward model is different
217 from a typical two-stream model in that the two-stream approximation is used only to calculate the
218 contribution of multiple scattering to the radiation field. Single scattering is treated in a numerically exact
219 manner using all moments of the phase function. This model has been used for remote sensing of
220 greenhouse gases and aerosols (Xi et al., 2015; Zhang et al., 2015, 2016; Zeng et al., 2017, 2018).
221 Aerosols are neither included in the forward model nor retrieved in this analysis. The surface albedo is
222 set to a wavelength-independent value of 0.5.

223 Results from the two retrieval methods reveal a similar CH₄ plume shape (Figure 4), especially for
224 elements with high CH₄ enhancement. However, larger differences in CH₄ concentrations are evident in
225 the OE retrievals (Figure 4b). Since radiance normalization reduces the impact of surface albedo and
226 aerosols are not included in either retrieval, this might be due to the fact that, in the OE method, H₂O and
227 CH₄ are simultaneously retrieved; the CH₄ retrieval has added uncertainty due to overlapping absorption
228 features between these two gases. The large maximum value of about 3000 in the MF method also
229 contributes to a reduction in relative contrast. While these results provide heuristic information about the
230 relative performance of the two retrieval techniques, it is difficult to compare the CH₄ enhancement
231 directly between the two methods since the background CH₄ concentration used in the MF method cannot
232 be quantified exactly. Further, evaluating retrieval biases due to ignoring aerosol scattering is not trivial
233 when real measurements are used. Therefore, we simulate synthetic spectra (see section 4) using the 2S-
234 ESS RT model to study the impacts of aerosol scattering as a function of different geophysical parameters
235 by varying them in a systematic manner.

236

237 **4 Aerosol impact analysis**

238 **4.1 Synthetic spectra**

239 In a real AVIRIS-NG observation, the exact column concentration of CH₄ cannot be controlled.
240 However, synthetic simulations allow us to manipulate parameters such as CH₄ concentration, surface
241 albedo, AOD, g , and SSA, and thereby test aerosol impacts on CH₄ retrievals. The 2S-ESS RT model is
242 used to simulate the AVIRIS-NG spectral radiance. In this model, a prior atmospheric profile with 70
243 layers from the surface up to 70 km is derived from National Center for Environmental Prediction
244 reanalysis data (Kalnay et al., 1996); absorption coefficients for all relevant gases are obtained from the
245 HITRAN database (Rothman et al., 2009). Monochromatic RT calculations are performed at a spectral
246 resolution of 0.5 cm⁻¹; the radiance spectrum is then convolved using a Gaussian instrument line shape
247 function with a wavelength-dependent full width at half maximum (FWHM) from a calibrated AVIRIS-
248 NG data file. The signal to noise ratio (SNR) is set to be 300, with Gaussian white noise added. This
249 procedure results in a wavelength grid with a resolution of about 5 nm. The spectral wavelength range
250 used to retrieve CH₄ is from 2100 nm to 2500 nm.

251 The additional atmospheric and geometric variables included in the model are listed in Table 3,
252 which are held constant unless otherwise mentioned. The observation geometry parameters are taken
253 from a real AVIRIS-NG measurement. Recent AVIRIS-NG flight campaigns have sensor heights ranging
254 from 0.43 to 3.8 km; we choose a value of 1 km, the same as the highest level where aerosol is present
255 in our simulations. The influence of AOD on CH₄ retrieval as a function of SSA and g is analyzed in
256 Section 4.3; in all other cases, SSA and g are held constant at 0.95 and 0.75, respectively, which is
257 representative of aerosols in the Los Angeles region (Zhang et al., 2015).

258 **4.2 Aerosol impact in the MF method**

259 We simulate synthetic spectra at different AOD, surface albedo and CH₄ concentration values, use
260 the MF method to obtain the CH₄ enhancement, and compare differences in α between scenarios without
261 and with aerosol. The covariance matrix and background mean radiance are calculated from a simulated
262 zero AOD background with surface albedos from 0.1 to 0.5, and XCH₄ set at the typical background
263 value of 1.822 ppm used in Section 3. Figure 5a shows the enhancement value as a function of XCH₄.
264 As the CH₄ concentration increases, the enhancement value obtained by the MF method at first increases
265 approximately linearly. However, the absorption changes in a nonlinear fashion with concentration,
266 whereas the MF method applies a linear formalism to the change. Therefore, the enhancement value
267 (which is correlated with the absorption signature) also shows a deviation from linear behavior at larger
268 XCH₄. Two aerosol scenarios (AOD = 0, 0.3) are compared in Figure 5a, which reveals that the effect of
269 aerosol loading is similar to an underestimation of CH₄ in the retrieval. The underestimation, which is

270 due to the shielding of CH₄ absorption below the aerosol layer and the fact that multiple scattering effects
271 between the aerosol and the surface are ignored, is clearly shown in Figure 5b, where the enhancement
272 value for fixed CH₄ concentration (same concentration as the background) decreases from 0 ppm × m
273 to -1532 ppm × m with increasing AOD. To clarify the impact of AOD at different surface albedo values,
274 zoomed in versions of α as a function of XCH₄ are presented in Figures 5c–f. For the AOD = 0 scenario,
275 the results are independent of surface albedo. This is because there are no multiple scattering effects
276 between the surface and the atmosphere (Rayleigh scattering is negligible in the retrieval wavelength
277 range) when there is no aerosol loading. For the scenarios with aerosol loading, the dispersion in the
278 zero-enhancement XCH₄ value between different surface albedos indicates that results from the MF
279 method are biased more at large AOD and surface albedo values (Figures 5d–f). This is a consequence
280 of increased multiple scattering between the aerosol layer and the surface that is not accounted for by the
281 retrieval algorithm. The maximum bias value is close to -700 ppm × m (equivalent to -0.06×1.822
282 ppm relative to the background concentration of 1.0×1.822 ppm) for an AOD of 0.3 and surface albedo
283 of 0.5 (Figure 5f). The implication of these results is that accurate knowledge of the surface albedo is
284 important for MF retrievals, especially when the aerosol loading is large.

285 A quantitative analysis of underestimation of CH₄ concentration due to aerosol scattering is
286 presented in Figure 6. The color bar shows the α bias — which is defined as the difference between the
287 enhancement value without aerosol (true α value) and that with aerosol — for different CH₄
288 concentrations, surface albedos and AODs. A positive bias means that CH₄ is underestimated. The α bias
289 increases with increasing surface albedo and AOD, reaching a maximum value of about 700 ppm × m
290 for the simulated cases. However, it is interesting that the bias decreases with increasing CH₄
291 concentration, which is different from the results obtained by the OE method (discussed in Section 4.3).
292 This surprising behavior is a direct consequence of the physical basis of the MF method. The rate of
293 increase in enhancement becomes smaller as XCH₄ becomes larger (Figure 5a). Therefore, at higher
294 XCH₄ values, the addition of aerosols (which has a similar effect as a reduction in XCH₄) results in a
295 lower reduction in enhancement compared to that at lower XCH₄ values, resulting in a net decrease in
296 the enhancement bias.

297 4.3 Aerosol impact in the OE method

298 For the simulation of the synthetic spectra, we assume nonzero aerosol loading below 1 km elevation.
299 The OE method is then used to perform retrievals using the same configuration (including, in particular,
300 the same surface albedo) except that AOD is set to zero. This approach is similar to neglecting aerosol
301 scattering in the CH₄ retrieval; the retrieval bias is defined as the difference between the true XCH₄ in
302 the simulation and the retrieved value (positive values refer to underestimation). First, we study the

303 retrieval bias caused by different aerosol types and mixtures. Figure 7a shows CH₄ retrieval biases as a
304 function of SSA and g ; surface albedo and AOD are kept constant at 0.3 and XCH₄ is assumed to be 1.0
305 \times 1.822 ppm. The retrieval bias increases with SSA and decreases with g , with a maximum bias ratio
306 (ratio of retrieval bias to the true value) of about 20%. This behavior can be explained as follows. At
307 higher SSA values, there are more multiple scattering effects (that are ignored in the retrieval). On the
308 other hand, larger values of g imply greater anisotropy of scattering (preference for forward scattering),
309 leading to a reduction in multiple scattering effects. Since the retrieval bias is large for high SSA and
310 low g , the water-soluble aerosol type (Table 1) and the maritime aerosol model (Table 2) can be expected
311 to induce greater biases in the retrieval. In order to compare the impacts of SSA and g in further detail,
312 retrieval results due to a \pm 5% change in SSA and g for the three aerosol models from Table 2 are shown
313 in Figures 7b and 7c. Note that for the maritime aerosol model, the SSA is set to 0.999 for the +5%
314 scenario to ensure physicality. It is clear that (1) the maritime aerosol model induces larger retrieval
315 biases than the other aerosol types, and (2) the retrieval results are more sensitive to changes in g than
316 those in SSA.

317 We then simulate synthetic spectra for different values of CH₄ concentration, surface albedo and
318 AOD. The impacts of aerosol scattering on the retrievals for these scenarios are demonstrated in Figure
319 8. Figure 8a shows a 5 \times 5 panel of boxes. Within each box, XCH₄ is constant, while surface albedo
320 increases from top to bottom and AOD increases from left to right. The variation of XCH₄ across the
321 boxes is shown in Figure 8b. We also show a zoomed in plot of the bottom right box (XCH₄ = 5.8 \times
322 1.822 ppm) in Figure 8c, which illustrates the AOD and surface albedo changes within a box. These
323 changes are identical for all boxes. Figure 8a indicates that OE retrievals produce larger CH₄ biases at
324 higher XCH₄ values, in contrast with MF results. In addition, it is evident that the retrieved CH₄ bias
325 increases with increasing AOD. The CH₄ bias induced by differences in the surface albedo is not as large
326 as that due to AOD variations, but surface albedo effects are noticeable at large AOD. Figure 8d shows
327 the sensitivity of retrieval biases to changes in AOD and surface albedo, again demonstrating the greater
328 impact of AOD than surface albedo in the retrieval.

329 The effects of changing the *a priori*, *a priori* error and RT simulation spectral resolution on the
330 retrieved XCH₄ are shown in Figure 9. For these calculations, the other parameters are set as follows:
331 SSA = 0.95, g = 0.75, AOD = 1.0, surface albedo = 0.5 and true XCH₄ = 5.8 \times 1.822ppm. The parameters
332 were chosen to correspond to the scenario with the largest retrieval bias in Figure 8c (bottom right box
333 in Figure 8c). Figure 9a shows that the retrieved XCH₄ changes by about 9 ppb as the *a priori* changes
334 from half to twice the true XCH₄ value. Similarly, the XCH₄ difference is less than 4 ppb when the *a*
335 *priori* error changes from 0.05 to 0.5 (Figure 9b). Compared to the bias of about 923 ppb induced by

336 neglecting aerosol scattering for this scenario, it is clear that the impacts of the *a priori* and *a priori* error
337 are very small. The effect of spectral resolution is larger, but XCH₄ still changes by only about 100 ppb
338 when the spectral resolution is changed from 0.5 to 0.1 cm⁻¹ (Figure 9c).

339 **4.4 Comparison of the two retrieval techniques**

340 Figure 10 presents the bias ratios for the two retrieval techniques at different AODs (surface albedo
341 = 0.3). In the MF method, the bias ratio is defined as the ratio of the bias to the true value of α . On the
342 other hand, in the OE method, it is the ratio of the bias to the true XCH₄. From Figure 10 it is clear that
343 the bias ratio decreases with increasing CH₄ concentration and has higher values at larger AODs. The
344 bias ratio for the MF method (1.3–4.5%) is up to 53.6% less than that for the OE method (2.8–5.6%) for
345 AOD = 0.3 when the CH₄ concentration is high (2–5 times typical background values). On the other
346 hand, the OE method performs better when enhancements are small and XCH₄ is close to the background
347 value. For example, the bias ratio for the MF method has a high value of about 42.6% at AOD = 0.3 for
348 a 10% enhancement (XCH₄ = 1.1 × 1.822 ppm); the OE value for the same scenario is 8.6%. For scenarios
349 where scattering is ignored, the two retrieval techniques seem to be complementary, with differing
350 utilities for different enhancements. On the other hand, when RT models that account for scattering
351 effects are employed, the MF technique is suboptimal. Further, MF retrievals rely on accurate
352 characterization of the surface albedo, especially when the aerosol loading is large. Finally, the MF
353 method does not retrieve concentrations, which are necessary to infer fluxes. Therefore, the OE technique
354 is in general superior due to its ability to support simultaneous retrieval of aerosols, surface albedo and
355 CH₄ concentration.

356

357 **5 Summary and discussion**

358 Remote sensing measurements from airborne and satellite instruments are widely used to detect
359 CH₄ emissions. In our study, the traditional MF and the OE methods are used to quantify the effects of
360 aerosol scattering on CH₄ retrievals based on simulations of AVIRIS-NG measurements. The results
361 show that the retrieval biases increase with increasing AOD and surface albedo for both techniques. In
362 the OE method the biases increase with increasing CH₄ concentration and SSA, but decrease with
363 increasing aerosol asymmetry parameter. The CH₄ retrieval bias increases with increasing XCH₄ in the
364 OE method but decreases for the same scenario in the MF method. The surprising MF trend is attributed
365 to the inability of the MF method to treat nonlinear absorption effects at high XCH₄ values. We also
366 present bias ratios for the two techniques. The MF method shows smaller bias ratios at large CH₄
367 concentrations than the OE method; it is, therefore, the optimal method to detect strong CH₄ emission
368 sources when scattering effects can be ignored in the retrieval. For the same retrieval scenario, the OE

369 method seems to be more suitable for detecting diffuse sources. Further, the MF method relies on a
370 comparison with the background CH₄ concentration. It is difficult to get an accurate estimate of the
371 background XCH₄ value in polluted atmospheric environments. In contrast, the OE method provides
372 retrievals based solely on the atmospheric scenario of interest; CH₄, aerosols and surface albedo can be
373 simultaneously inferred. Therefore, when scattering effects need to be considered, the OE method is the
374 appropriate choice. Indeed, the MF method was intended for plume detection. OE enables accurate
375 quantification of XCH₄ in the presence of aerosol scattering.

376 This study focused on a comparison of retrieval techniques. It is also important to accurately
377 represent the physics of atmospheric RT, especially for scenarios with significant aerosol scattering. RT
378 models traditionally used in retrievals of imaging spectroscopic data use simplified radiation schemes
379 and predefined aerosol models, which may introduce inaccuracies in the representation of atmospheric
380 physics. The 2S-ESS model provides the capability to quantify aerosol impacts on CH₄ retrieval for
381 different aerosol types, optical depths and layer heights. In future work, we will compare retrievals using
382 the 2S-ESS model against those from other commonly used models such as MODTRAN. We will also
383 evaluate the impact of varying instrument spectral resolution and signal to noise ratio for simultaneous
384 retrieval of CH₄, surface albedo and AOD. This will be relevant for the design of imaging spectrometers
385 for planned future missions such as the NASA Surface Biology and Geology (SBG) mission.

386

387 **Data availability**

388 The code and data are available from the authors upon request.

389

390 **Author contributions**

391 VN conceived the work, provided the radiative transfer and aerosol models, supervised YH, and
392 assisted with manuscript preparation. YH designed and performed the retrievals, analyzed the results,
393 and prepared the original manuscript. ZZ contributed to retrieval setup and assisted with analysis of the
394 results. PK provided valuable inputs into the science of CH₄ remote sensing. YLY supervised YH and
395 participated in the evaluation of the retrieval results and intercomparison. All listed authors contributed
396 to the review and editing of this manuscript.

397

398 **Competing interests**

399 The authors declare that they have no conflict of interest.

400

401 **Acknowledgements**

402 A portion of this research was carried out at the Jet Propulsion Laboratory, California Institute of
403 Technology, under a contract with the National Aeronautics and Space Administration
404 (80NM0018D0004). The authors gratefully acknowledge the insightful and constructive comments from
405 the two anonymous reviewers, which improved the clarity and quality of the manuscript, and elevated
406 the significance of the work beyond the original expectation.

407

408 **Financial Support**

409 VN acknowledges support from the NASA “Utilization of Airborne Visible/Infrared Imaging
410 Spectrometer Next Generation Data from an Airborne Campaign in India” program (solicitation
411 NNH16ZDA001N-AVRSNG), and the Jet Propulsion Laboratory Research and Technology
412 Development program. PK was funded by the Japan Society for the Promotion of Science International
413 Research Fellow Program.

414

415 **References**

416

417 Alvarez, R. A., Zavala-Araiza, D., Lyon, D. R., Allen, D. T., Barkley, Z. R., Brandt, A. R., Davis, K. J.,
418 Herndon, S. C., Jacob, D. J., Karion, A., Kort, E. A., Lamb, B. K., Lauvaux, T., Maasakkers, J. D.,
419 Marchese, A. J., Omara, M., Pacala, S. W., Peischl, J., Robinson, A. L., Shepson, P. B., Sweeney, C.,
420 Townsend-Small, A., Wofsy, S. C., and Hamburg, S. P.: Assessment of methane emissions from the U.S.
421 oil and gas supply chain, *Science*, 361, 186–188, <https://doi.org/10.1126/science.aar7204>, 2018.

422

423 Archer, D.: Methane hydrate stability and anthropogenic climate change, *Biogeosci.*, 4, 521–544,
424 <https://doi.org/10.5194/bg-4-521-2007>, 2007.

425

426 Bradley, E. S., Leifer, I., Roberts, D. A., Dennison, P. E., and Washburn, L.: Detection of marine methane
427 emissions with AVIRIS band ratios, *Geophys. Res. Lett.*, 38, L10702,
428 <https://doi.org/10.1029/2011GL046729>, 2011.

429

430 Bubier, J. L., and Moore, T. R: An ecological perspective on methane emissions from northern wetlands,
431 *Trends in Ecology and Evolution*, 9, 460–464, [https://doi.org/10.1016/0169-5347\(94\)90309-3](https://doi.org/10.1016/0169-5347(94)90309-3), 1994.

432

433 Buchwitz, M., Reuter, M., Bovensmann, H., Pillai, D., Heymann, J., Schneising, O., Rozanov, V., Krings,
434 T., Burrows, J. P., Boesch, H., Gerbig, C., Meijer, Y., and Löscher, A.: Carbon Monitoring Satellite
435 (CarbonSat): Assessment of atmospheric CO₂ and CH₄ retrieval errors by error parameterization, *Atmos.*
436 *Meas. Tech.*, 6, 3477–3500, <https://doi.org/10.5194/amt-6-3477-2013>, 2013.

437

438 Butz, A., Galli, A., Hasekamp, O., Landgraf, J., Tol, P., and Aben, I.: TROPOMI aboard Sentinel-5
439 Precursor: Prospective performance of CH₄ retrievals for aerosol and cirrus loaded atmospheres, *Remote*
440 *Sens. Environ.*, 120, 267–276, <https://doi.org/10.1016/j.rse.2011.05.030>, 2012.

441

442 Butz, A., Orphal, J., Checa-Garcia, R., Friedl-Vallon, F., von Clarmann, T., Bovensmann, H., Hasekamp,
443 O., Landgraf, J., Knigge, T., Weise, D., Sqalli-Houssini, O., and Kemper, D.: Geostationary Emission
444 Explorer for Europe (G3E): Mission concept and initial performance assessment, *Atmos. Meas. Tech.*, 8,
445 4719–4734, <https://doi.org/10.5194/amt-8-4719-2015>, 2015.

446

447 Clerbaux, C., Hadji-Lazaro, J., Turquety, S., Mégie, G., and Coheur, P.-F.: Trace gas measurements from
448 infrared satellite for chemistry and climate applications, *Atmos. Chem. Phys.*, 3, 1495–1508,
449 <https://doi.org/10.5194/acp-3-1495-2003>, 2003.

450

451 Dennison, P. E., Thorpe, A. K., Pardyjak, E. R., Roberts, D. A., Qi, Y., Green, R. O., Bradley, E. S., and
452 Funk, C. C.: High spatial resolution mapping of elevated atmospheric carbon dioxide using airborne
453 imaging spectroscopy: Radiative transfer modeling and power plant plume detection, *Remote Sens.*
454 *Environ.*, 139, 116-129, <https://doi.org/10.1016/j.rse.2013.08.001>, 2013.

455

456 Etiope, G., Feyzullayev, A., and Baciu, C. L.: Terrestrial methane seeps and mud volcanoes: A global
457 perspective of gas origin, *Mar. Pet. Geol.*, 26, 333–344, <https://doi.org/10.1016/j.marpetgeo.2008.03.001>,
458 2009.

459

460 Fishman, J. L., Iraci, L. T., Al-Saadi, J., Chance, K., Chavez, F., Chin, M., Coble, P., Davis, C.,
461 DiGiacomo, P. M., Edwards, D., Eldering, A., Goes, J., Herman, J., Hu, C., Jacob, D. J., Jordan, C., Kawa,
462 S. R., Key, R., Liu, X., Lohrenz, S., Mannino, A., Natraj, V., Neil, D., Neu, J., Newchurch, M., Pickering,
463 K., Salisbury, J., Sosik, H., Subramaniam, A., Tzortziou, M., Wang, J., and Wang, M.: The United States’
464 next generation of atmospheric composition and coastal ecosystem measurements: NASA’s
465 Geostationary Coastal and Air Pollution Events (GEO-CAPE) Mission, *Bull. Am. Meteorol. Soc.*,
466 <https://doi.org/10.1175/BAMS-D-11-00201.1>, 2012.

467

468 Frankenberg, C., Platt, U., and Wagner, T.: Iterative maximum a posteriori (IMAP)-DOAS for retrieval
469 of strongly absorbing trace gases: Model studies for CH₄ and CO₂ retrieval from near infrared spectra of
470 SCIAMACHY onboard ENVISAT, *Atmos. Chem. Phys.*, 5, 9–22, <https://doi.org/10.5194/acp-5-9-2005>,
471 2005.

472

473 Frankenberg, C., Meirink, J. F., Bergamaschi, P., Goede, A., P. H., Heimann, M., Körner, S., Platt, U.,
474 van Weele, M., and Wagner, T.: Satellite cartography of atmospheric methane from SCIAMACHY on
475 board ENVISAT: Analysis of the years 2003 and 2004, *J. Geophys. Res.*, 111, D07303,
476 <https://doi.org/10.1029/2005JD006235>, 2006.

477

478 Frankenberg, C., Thorpe, A. K., Thompson, D. R., Hulley, G., Kort, E. A., Vance, N., Borchardt, J.,
479 Krings, T., Gerilowski, K., Sweeney, C., Conley, S., Bue, B. D., Aubrey, A. D., Hook, S., and Green, R.

480 O.: Airborne methane remote measurements reveal heavy-tail flux distribution in Four Corners region,
481 Proc. Natl. Acad. Sci. U. S. A., 113, 9734–9739, <https://doi.org/10.1073/pnas.1605617113>, 2016.

482

483 Gambacorta, A., Barnet, C. D., Smith, N., Pierce, R. B., Smith, J. W., Spackman, J. R., and Goldberg,
484 M.: The NPP and J1 NOAA Unique Combined Atmospheric Processing System (NUCAPS) for
485 atmospheric thermal sounding: Recent algorithm enhancements tailored to near real time users
486 applications, Abstract IN33D-07, presented at 2016 Fall Meeting, AGU, San Francisco, CA, 12–16 Dec.,
487 2016.

488

489 Gedney, N., Cox, P. M., and Huntingford, C.: Climate feedback from wetland methane emissions,
490 Geophys. Res. Lett., 31, L20503. <https://doi.org/10.1029/2004GL020919>, 2004.

491

492 Glumb, R., Davis, G., and Lietzke, C.: The TANSO-FTS-2 instrument for the GOSAT-2 greenhouse gas
493 monitoring mission, 2014 IEEE Geoscience and Remote Sensing Symposium, Quebec City, QC, 1238–
494 1240, <https://doi.org/10.1109/IGARSS.2014.6946656>, 2014.

495

496 Green, R. O., Eastwood, M. L., Sarture, C. M., Chrien, T. G., Aronsson, M., Chippendale, B. J., Faust,
497 J. A., Pavri, B. E., Chovit, C. J., Solis, M., Olah, M. R., and Williams, O.: Imaging spectroscopy and the
498 Airborne Visible/Infrared Imaging Spectrometer (AVIRIS), Remote Sens. Environ., 65, 227–248,
499 [https://doi.org/10.1016/S0034-4257\(98\)00064-9](https://doi.org/10.1016/S0034-4257(98)00064-9), 1998.

500

501 He, L., Zeng, Z.-C., Pongetti, T. J., Wong, C., Liang, J., Gurney, K. R., Newman, S., Yadav, V., Verhulst,
502 K., Miller, C. E., and Duren, R.: Atmospheric methane emissions correlate with natural gas consumption
503 from residential and commercial sectors in Los Angeles, Geophys. Res. Lett., 46, 8563–8571,
504 <https://doi.org/10.1029/2019GL083400>, 2019.

505

506 Henyey, L. G., and Greenstein, J. L.: Diffuse radiation in the galaxy, Astrophys. J., 93, 70–83,
507 <https://doi.org/10.1086/144246>, 1941.

508

509 Herrero, M., Henderson, B., Havlik, P., Thornton, P. K., Conant, R. T., Smith, P., Wirseniuss, S., Hristov,
510 A. N., Gerber, P., Gill, M., Butterbach-Bahl, K., Valin, H., Garnett, T., and Shehfest, E.: Greenhouse gas
511 mitigation potentials in the livestock sector, Nature Clim. Change, 6, 452–461,
512 <https://doi.org/10.1038/nclimate2925>, 2016.

513 Holmes, C. D., Prather, M. J., Søvde, O. A., and Myhre, G.: Future methane, hydroxyl, and their
514 uncertainties: key climate and emission parameters for future predictions, *Atmos. Chem. Phys.*, 13, 285–
515 302, <https://doi.org/10.5194/acp-13-285-2013>, 2013.

516

517 Howarth, R. W.: Methane emissions and climatic warming risk from hydraulic fracturing and shale gas
518 development: implications for policy, *Energy and Emission Control Technologies*, 3, 45–54,
519 <https://doi.org/10.2147/EECT.S61539>, 2015.

520

521 Howarth, R. W.: Ideas and perspectives: is shale gas a major driver of recent increase in global
522 atmospheric methane?, *Biogeosciences*, 16, 3033–3046, <https://doi.org/10.5194/bg-16-3033-2019>, 2019.

523

524 Howarth, R. W., Santoro, R., and Ingraffea, A.: Methane and the greenhouse gas footprint of natural gas
525 from shale formations, *Clim. Change*, 106, 679, <https://doi.org/10.1007/s10584-011-0061-5>, 2011.

526

527 Jacob, D. J., Turner, A. J., Maasakkers, J. D., Sheng, J., Sun, K., Liu, X., Chance, K., Aben, I., McKeever,
528 J., and Frankenberg, C.: Satellite observations of atmospheric methane and their value for quantifying
529 methane emissions, *Atmos. Chem. Phys.*, 16, 14371–14396, <https://doi.org/10.5194/acp-16-14371-2016>,
530 2016.

531

532 Jervis, D., McKeever, J., Durak, B. O. A., Sloan, J. J., Gains, D., Varon, D. J., Ramier, A., Strupler, M.,
533 and Tarrant, E.: The GHGSat-D imaging spectrometer, *Atmos. Meas. Tech. Discuss.*,
534 <https://doi.org/10.5194/amt-2020-301>, in review, 2020.

535

536 Kalnay, E., Kanamitsu, M., Kistler, R., Collins, W., Deaven, D., Gandin, L., Iredell, M., Saha, S., White,
537 G., Woollen, J., Zhu, Y., Chelliah, M., Ebisuzaki, W., Higgins, W., Janowiak, J., Mo, K. C., Ropelewski,
538 C., Wang, J., Leetmaa, A., Reynolds, R., Jenne, R., and Joseph, D.: The NCEP/NCAR 40-year reanalysis
539 project, *Bull. Am. Meteorol. Soc.*, 77, 437–471, [https://doi.org/10.1175/1520-
540 0477\(1996\)077<0437:TNYRP>2.0.CO;2](https://doi.org/10.1175/1520-0477(1996)077<0437:TNYRP>2.0.CO;2), 1996.

541

542 Kiemle, C., Kawa, S. R., Quatrevalet, M., and Browell, E. V.: Performance simulations for a spaceborne
543 methane lidar mission, *J. Geophys. Res.*, 119, 4365–4379, <https://doi.org/10.1002/2013JD021253>, 2014.

544

545 Kirschke, S., Bousquet, P., Ciais, P., Saunois, M., Canadell, Josep G., Dlugokencky, E. J., Bergamaschi,
546 P., Bergmann, D., Blake, D. R., Bruhwiler, L., Cameron-Smith, P., Castaldi, S., Chevallier, F., Feng, L.,
547 Fraser, A., Heimann, M., Hodson, E. L., Houweling, S., Josse, B., Fraser, P. J., Krummel, P. B., Lamarque,
548 J.-F., Langenfelds, R. L., Le Quere, C., Naik, V., O'Doherty, S., Palmer, P. I., Pison, I., Plummer, D.,
549 Poulter, B., Prinn, R. G., Rigby, M., Ringeval, B., Santini, M. Schmidt, M., Shindell, D. T., Simpson, I.
550 J., Spahni, R., Steele, L. P., Strode, S. A., Sudo, K., Szopa, S., van der Werf, G. R., Voulgarakis, A., van
551 Weele, M., Weiss, R. F., Williams, J. E., and Zeng, G.: Three decades of global methane sources and
552 sinks, *Nature Geosci.*, 6, 813–823, <https://doi.org/10.1038/ngeo1955>, 2013.

553

554 Kort, E. A., Frankenberg, C., Costigan, K. R., Lindenmaier, R., Dubey, M. K., and Wunch, D.: Four
555 corners: the largest US methane anomaly viewed from space, *Geophys. Res. Lett.*, 41, 6898–6903,
556 <https://doi.org/10.1002/2014GL061503>, 2014.

557

558 Kuze, A., Suto, H., Shiomi, K., Kawakami, S., Tanaka, M., Ueda, Y., Deguchi, A., Yoshida, J., Yamamoto,
559 Y., Kataoka, F., Taylor, T. E., and Buijs, H. L.: Update on GOSAT TANSO-FTS performance, operations,
560 and data products after more than 6 years in space, *Atmos. Meas. Tech.*, 9, 2445–2461,
561 <https://doi.org/10.5194/amt-9-2445-2016>, 2016.

562

563 Kvenvolden, K. A.: Methane hydrate – A major reservoir of carbon in the shallow geosphere, *Chem.*
564 *Geol.*, 71, 41–51, [https://doi.org/10.1016/0009-2541\(88\)90104-0](https://doi.org/10.1016/0009-2541(88)90104-0), 1988.

565

566 Kvenvolden, K. A., and Rogers, B. W.: Gaia's breath – global methane exhalations, *Mar. Pet. Geol.*, 22,
567 579–590, <https://doi.org/10.1016/j.marpetgeo.2004.08.004>, 2005.

568

569 Macdonald, J. A., Fowler, D., Hargreaves, K. J., Skiba, U., Leith, I. D., and Murray, M. B.: Methane
570 emission rates from a northern wetland; response to temperature, water table and transport, *Atmos.*
571 *Environ.*, 32, 3219–3227, [https://doi.org/10.1016/S1352-2310\(97\)00464-0](https://doi.org/10.1016/S1352-2310(97)00464-0), 1998.

572

573 Manolakis, D., Truslow, E., Pieper, M., Cooley, T., and Brueggeman, M.: Detection algorithms in
574 hyperspectral imaging systems: An overview of practical algorithms, *IEEE Signal Proc. Mag.*, 31, 24–
575 33, <https://doi.org/10.1109/MSP.2013.2278915>, 2014.

576

577 McKeever, J., Durak, B. O. A., Gains, D., Varon, D. J., Germain, S., and Sloan, J. J.: GHGSat-D:
578 Greenhouse gas plume imaging and quantification from space using a Fabry-Perot imaging spectrometer,
579 Abstract A33G-1360 presented at 2017 Fall Meeting, AGU, New Orleans, LA, 11–15 December, 2017.
580

581 Merchant, C. J., Le Borgne, P., Roquet, H., and Legendre, G.: Extended optimal estimation techniques
582 for sea surface temperature from the Spinning Enhanced Visible and Infra-Red Imager (SEVIRI),
583 Remote Sens. Environ., 131, 287–297, <https://doi.org/10.1016/j.rse.2012.12.019>, 2013.
584

585 Myhre, G., Shindell, D., Bréon, F.-M., Collins, W., Fuglestedt, J., Huang, J., Koch, D., Lamarque, J.-
586 F., Lee, D., Mendoza, B., Nakajima, T., Robock, A., Stephens, G., Takemura, T., and Zhang, H.:
587 Anthropogenic and Natural Radiative Forcing, Climate Change 2013: The Physical Science Basis.
588 Contribution of Working Group I to the Fifth Assessment Report of the Intergovernmental Panel on
589 Climate Change – IPCC, 2013.
590

591 Nisbet, E. G., Dlugokencky, E. J., and Bousquet, P.: Methane on the rise-Again, Science, 343, 493–495,
592 <https://doi.org/10.1126/science.1247828>, 2014.
593

594 Nisbet, E. G., Dlugokencky, E. J., Manning, M. R., Lowry, D., Fisher, R. E., France, J. L., Michel, S. E.,
595 Miller, J. B., White, J. W. C., Vaughn, B., Bousquet, P., Pyle, J. A., Warwick, N. J., Cain, M., Brownlow,
596 R., Zazzeri, G., Lanoisellé, M., Manning, A. C., Gloor, E., Worthy, D. E. J., Brunke, E.-G., Labuschagne,
597 C., Wolff, E. W., and Ganesan, A. L.: Rising atmospheric methane: 2007–2014 growth and isotopic shift,
598 Glob. Biogeochem. Cycles, 30, 1356–1370, <https://doi.org/10.1002/2016GB005406>, 2016.
599

600 NOAA Earth System Research Laboratory Global Monitoring Laboratory,
601 https://esrl.noaa.gov/gmd/ccgg/trends_ch4/, 2019.
602

603 O’Dell, C. W., Eldering, A., Wennberg, P. O., Crisp, D., Gunson, M. R., Fisher, B., Frankenberg, C.,
604 Kiel, M., Lindqvist, H., Mandrake, L., Merrelli, A., Natraj, V., Nelson, R. R., Osterman, G. B., Payne,
605 V. H., Taylor, T. E., Wunch, D., Drouin, B. J., Oyafuso, F., Chang, A., McDuffie, J., Smyth, M., Baker,
606 D. F., Basu, S., Chevallier, F., Crowell, S. M. R., Feng, L., Palmer, P. I., Dubey, M., García, O. E.,
607 Griffith, D. W. T., Hase, F., Iraci, L. T., Kivi, R., Morino, I., Notholt, J., Ohyama, H., Petri, C., Roehl,
608 C. M., Sha, M. K., Strong, K., Sussmann, R., Te, Y., Uchino, O. and Velasco, V. A.: Improved retrievals

609 of carbon dioxide from Orbiting Carbon Observatory-2 with the version 8 ACOS algorithm, *Atmos.*
610 *Meas. Tech.*, 11(12), 6539–6576, <https://doi.org/10.5194/amt-11-6539-2018>, 2018.

611

612 Polonsky, I. N., O’Brien, D. M., Kumer, J. B., O’Dell, C. W., and the geoCARB Team: Performance of
613 a geostationary mission, geoCARB, to measure CO₂, CH₄ and CO column-averaged concentrations,
614 *Atmos. Meas. Tech.*, 7, 959–981, <https://doi.org/10.5194/amt-7-959-2014>, 2014.

615

616 Roberts, D. A., Bradley, E. S., Cheung, R., Leifer, I., Dennison, P. E., and Margolis, J. S.: Mapping
617 methane emissions from a marine geological seep source using imaging spectrometry, *Remote Sens.*
618 *Environ.*, 114, 592–606, <https://doi.org/10.1016/j.rse.2009.10.015>, 2010.

619

620 Rodgers, C. D.: *Inverse Methods for Atmospheric Sounding: Theory and Practice*, World Scientific,
621 Singapore, 2000.

622

623 Rothman, L. S., Gordon, I. E., Barbe, A., Benner, D. C., Bernath, P. E., Birk, M., Boudon, V., Brown,
624 L. R., Campargue, A., Champion, J. P., Chance, K., Coudert, L. H., Dana, V., Devi, V. M., Fally, S.,
625 Flaud, J. M., Gamache, R. R., Goldman, A., Jacquemart, D., Kleiner, I., Lacome, N., Lafferty, W. J.,
626 Mandin, J. Y., Massie, S. T., Mikhailenko, S. N., Miller, C. E., Moazzen-Ahmadi, N., Naumenko, O. V.,
627 Nikitin, A. V., Orphal, J., Perevalov, V. I., Perrin, A., Predoi-Cross, A., Rinsland, C. P., Rotger, M.,
628 Šimečková, M., Smith, M. A. H., Sung, K., Tashkun, S. A., Tennyson, J., Toth, R. A., Vandaele, A. C.,
629 and Vander Auwera, J.: The HITRAN 2008 molecular spectroscopic database, *J. Quant. Spectrosc.*
630 *Radiat. Transfer*, 110, 533–572, <https://doi.org/10.1016/j.jqsrt.2009.02.013>, 2009.

631

632 Schaefer, H., Fletcher, S. E. M., Veidt, C., Lassey, K. R., Brailsford, G. W., Bromley, T. M.,
633 Dlugokencky, E. J., Michel, S. E., Miller, J. M., Levin, I., Lowe, D. C., Martin, R. J., Vaughn, B. H., and
634 White, J. W. C.: A 21st-century shift from fossil-fuel to biogenic methane emissions indicated by ¹³CH₄,
635 *Science*, 352, 80-84, <https://doi.org/10.1126/science.aad2705>, 2016.

636

637 Schaefer, K., Lantuit, H., Romanovsky, V. E., Schuur, E. A. G., and Witt, R.: The impact of the
638 permafrost carbon feedback on global climate, *Environ. Res. Lett.*, 9, 085003,
639 <https://doi.org/10.1088/1748-9326/9/8/085003>, 2014.

640

641 Schuur, E. A. G., McGuire, A. D., Schädel, C., Grosse, G., Harden, J. W., Hayes, D. J., Hugelius, G.,
642 Koven, C. D., Kuhry, P., Lawrence, D. M., Natali, S. M., Olefeldt, D., Romanovsky, V. E., Schaefer, K.,
643 Turetsky, M. R., Treat, C. C., and Vonk, J. E.: Climate change and the permafrost carbon feedback,
644 *Nature*, 520, 171–179, <https://doi.org/10.1038/nature14338>, 2015.

645

646 Seinfeld, J. H., and Pandis, S. N.: *Atmospheric Chemistry and Physics: From Air Pollution to Climate*
647 *Change*, Wiley, New Jersey, USA, 2006.

648

649 Spurr, R., and Natraj, V.: A linearized two-stream radiative transfer code for fast approximation of
650 multiple-scatter fields, *J. Quant. Spectrosc. Radiat. Transfer*, 112, 2630–2637,
651 <https://doi.org/10.1016/j.jqsrt.2011.06.014>, 2011.

652

653 Themelis, N. J., and Ulloa, P. A.: Methane generation in landfills, *Renewable Energy*, 32, 1243–1257,
654 <https://doi.org/10.1016/j.renene.2006.04.020>, 2007.

655

656 Thompson, D. R., Leifer, I., Bovensmann, H., Eastwood, M., Fladland, M., Frankenberg, C.,
657 Gerilowski, K., Green, R. O., Kratwurst, S., Krings, T., Luna, B., and Thorpe, A. K.: Real-time remote
658 detection and measurement for airborne imaging spectroscopy: a case study with methane, *Atmos. Meas.*
659 *Tech.*, 8, 4383–4397, <https://doi.org/10.5194/amt-8-4383-2015>, 2015.

660

661 Thorpe, A. K., Frankenberg, C., and Roberts, D. A.: Retrieval techniques for airborne imaging of
662 methane concentrations using high spatial and moderate spectral resolution: Application to AVIRIS,
663 *Atmos. Meas. Tech.*, 7, 491–506, <https://doi.org/10.5194/amt-7-491-2014>, 2014.

664 Thorpe, A. K., Roberts, D. A., Bradley, E. S., Funk, C. C., Dennison, P. E., and Leifer, I.: High resolution
665 mapping of methane emissions from marine and terrestrial sources using a Cluster-Tuned Matched Filter
666 technique and imaging spectrometry, *Remote Sens. Environ.*, 134, 305–318,
667 <https://doi.org/10.1016/j.rse.2013.03.018>, 2013.

668

669 Varon, D. J., McKeever, J., Jervis, D., Maasackers, J. D., Pandey, S., Houweling, S., Aben, I., Scarpelli,
670 T. and Jacob, D. J.: Satellite discovery of anomalously large methane point sources from oil/gas
671 production, *Geophys. Res. Lett.*, 2019.

672

673 Veefkind, J. P., Aben, I., McMullan, K., Forster, H., de Vries, J., Otter, G., Claas, J., Eskes, H. J., de Haan,
674 J. F., Kleipool, Q., van Weele, M., Hasekamp, O., Hoogeveen, R., Landgraf, J., Snel, R., Tol, P., Ingmann,
675 P., Voors, R., Kruizinga, B., Vink, R., Visser, H., and Levelt, P. F.: TROPOMI on the ESA Sentinel-5
676 Precursor: A GMES mission for global observations of the atmospheric composition for climate, air
677 quality and ozone layer applications, *Remote Sens. Environ.*, 120, 70–83,
678 <https://doi.org/10.1016/j.rse.2011.09.027>, 2012.

679

680 Walter, K. M., Zimov, S. A., Chanton, J. P., Verbyla, D., and Chapin III, F. S.: Methane bubbling from
681 Siberian thaw lakes as a positive feedback to climate warming, *Nature*, 443, 71–75,
682 <https://doi.org/10.1038/nature05040>, 2006.

683

684 Wofsy, S. C., and Hamburg, S.: MethaneSAT — A new observing platform for high resolution
685 measurements of methane and carbon dioxide, Abstract A53F-02 presented at 2019 Fall Meeting, AGU,
686 San Francisco, CA, 9–13 December, 2019.

687

688 World Climate Research Program (WCRP): A preliminary cloudless standard atmosphere for radiation
689 computation, International Association for Meteorology and Atmospheric Physics, Radiation
690 Commission, Boulder, CO, USA, 1984, CSP-112, WMO/TD-No. 24, March 1986.

691

692 Woodwell, G. M., Mackenzie, F. T., Houghton, R. A., Apps, M., Gorham, E., and Davidson, E.: Biotic
693 feedbacks in the warming of the earth, *Climatic Change*, 40, 495–518,
694 <https://doi.org/10.1023/A:1005345429236>, 1998.

695

696 Worden, J., Kulawik, S., Frankenberg, C., Payne, V., Bowman, K., Cady-Peirara, K., Wecht, K., Lee, J.-
697 E., and Noone, D.: Profiles of CH₄, HDO, H₂O, and N₂O with improved lower tropospheric vertical
698 resolution from Aura TES radiances, *Atmos. Meas. Tech.*, 5, 397–411, [https://doi.org/10.5194/amt-5-](https://doi.org/10.5194/amt-5-397-2012)
699 [397-2012](https://doi.org/10.5194/amt-5-397-2012), 2012.

700

701 Xi, X., Natraj, V., Shia, R. L., Luo, M., Zhang, Q., Newman, S., Sander, S. P., and Yung, Y. L.: Simulated
702 retrievals for the remote sensing of CO₂, CH₄, CO, and H₂O from geostationary orbit, *Atmos. Meas.*
703 *Tech.*, 8, 4817–4830, <https://doi.org/10.5194/amtd-8-5809-2015>, 2015.

704

705 Xiong, X., Barnet, C., Maddy, E., Sweeney, C., Liu, X., Zhou, L., and Goldberg, M.: Characterization
706 and validation of methane products from the Atmospheric Infrared Sounder (AIRS), *J. Geophys. Res.*,
707 113, G00A01, <https://doi.org/10.1029/2007JG000500>, 2008.

708

709 Xiong, X., Barnet, C., Maddy, E. S., Gambacorta, A., King, T. S., and Wofsy, S. C.: Mid-upper
710 tropospheric methane retrieval from IASI and its validation, *Atmos. Meas. Tech.*, 6, 2255–2265,
711 <https://doi.org/10.5194/amt-6-2255-2013>, 2013.

712

713 Yoshida, Y., Kikuchi, N., Morino, I., Uchino, O., Oshchepkov, S., Bril, A., Saeki, T., Schutgens, N.,
714 Toon, G. C., Wunch, D., Roehl, C. M., Wennberg, P. O., Griffith, D. W. T., Deutscher, N. M., Warneke,
715 T., Notholt, J., Robinson, J., Sherlock, V., Connor, B., Rettinger, M., Sussmann, R., Ahonen, P.,
716 Heikkinen, P., Kyrö, E., Mendonca, J., Strong, K., Hase, F., Dohe, S., and Yokota, T.: Improvement of
717 the retrieval algorithm for GOSAT SWIR XCO₂ and XCH₄ and their validation using TCCON data,
718 *Atmos. Meas. Tech.*, 6, 1533–1547, <https://doi.org/10.5194/amt-6-1533-2013>, 2013.

719

720 Zeng, Z.-C., Zhang, Q., Natraj, V., Margolis, J. S., Shia, R. -L., Newman, S., Fu, D., Pongetti, T. J.,
721 Wong, K. W., Sander, S. P., Wennberg, P. O., and Yung, Y. L.: Aerosol scattering effects on water vapor
722 retrievals over the Los Angeles Basin, *Atmos. Chem. Phys.*, 17, 2495–2508, [https://doi.org/10.5194/acp-](https://doi.org/10.5194/acp-17-2495-2017)
723 [17-2495-2017](https://doi.org/10.5194/acp-17-2495-2017), 2017.

724

725 Zeng, Z.-C., Natraj, V., Xu, F., Pongetti, T. J., Shia, R.-L., Kort, E. A., Toon, G. C., Sander, S. P., and
726 Yung, Y. L.: Constraining aerosol vertical profile in the boundary layer using hyperspectral
727 measurements of oxygen absorption, *Geophys. Res. Lett.*, 45, 10772–10780,
728 <https://doi.org/10.1029/2018GL079286>, 2018.

729

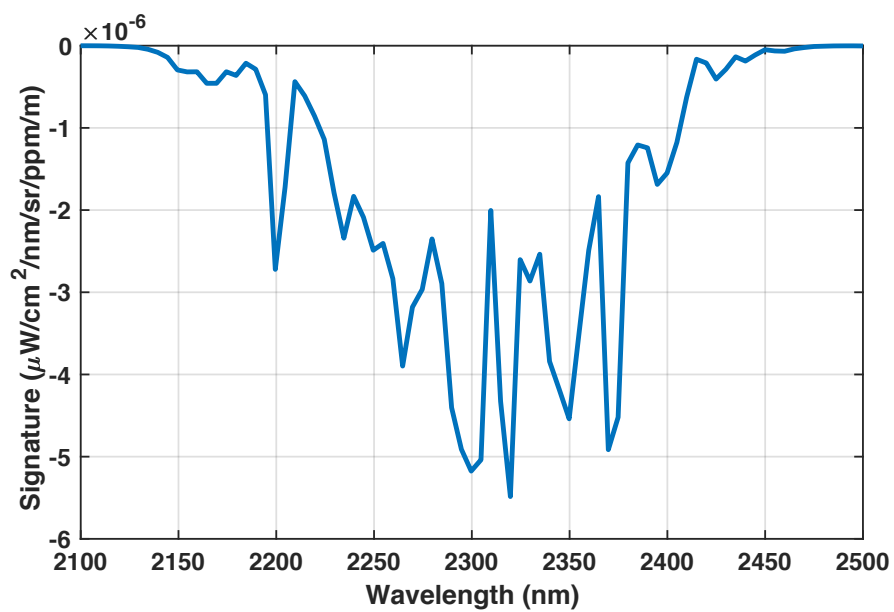
730 Zhang, Q., Natraj, V., Li, K. -F., Shia, R. -L., Fu, D., Pongetti, T. J., Sander S. P., Roehl, C. M., and
731 Yung, Y. L.: Accounting for aerosol scattering in the CLARS retrieval of column averaged CO₂ mixing
732 ratios, *J. Geophys. Res.*, 120, 7205–7218, <https://doi.org/10.1002/2015JD023499>, 2015.

733

734 Zhang, Q., Shia, R. -L., Sander, S. P., and Yung, Y. L.: XCO₂ retrieval error over deserts near critical
735 surface albedo, *Earth Space Sci.*, 2, 1–10, <https://doi.org/10.1002/2015EA000143>, 2016.

736

737



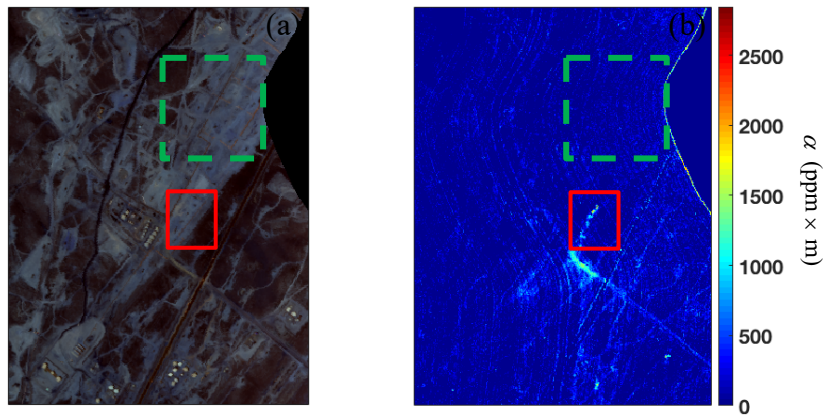
738

739

740 **Figure 1: The target signature used for the Matched Filter method.**

741

742

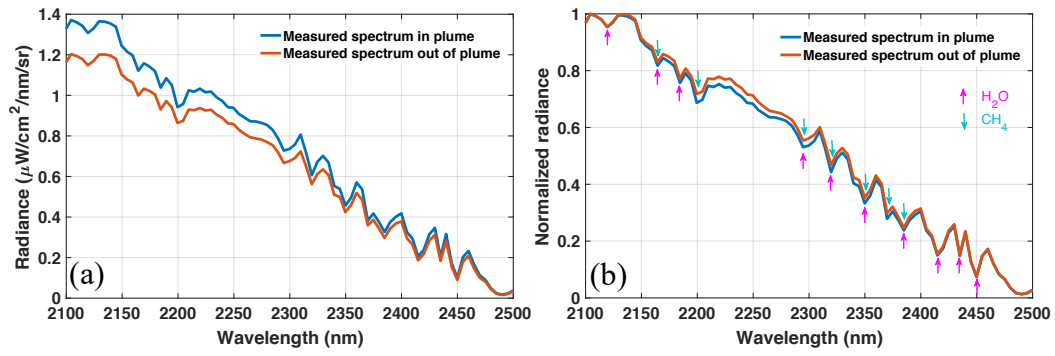


743

744 **Figure 2: (a) RGB image of flight data from 4 September 2014 (ang20140904t204546). Adapted from**
745 **Thompson et al. (2015). (b) CH₄ enhancement value α (ppm \times m) obtained by the MF method. An emission**
746 **source is shown in the solid red box and the background region near the target for the MF calculation is**
747 **indicated by the dashed green box.**

748

749



750

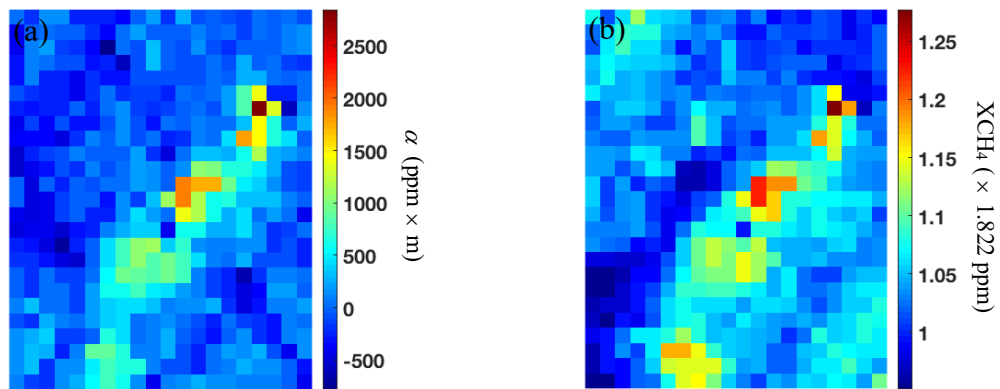
751 **Figure 3: (a) Real radiance and (b) normalized radiance at cross-track detector elements (in and out of plume)**

752 **from the sample AVIRIS-NG measurement. The colored arrows in (b) show the main absorption features due**

753 **to H_2O (purple) and CH_4 (green).**

754

755

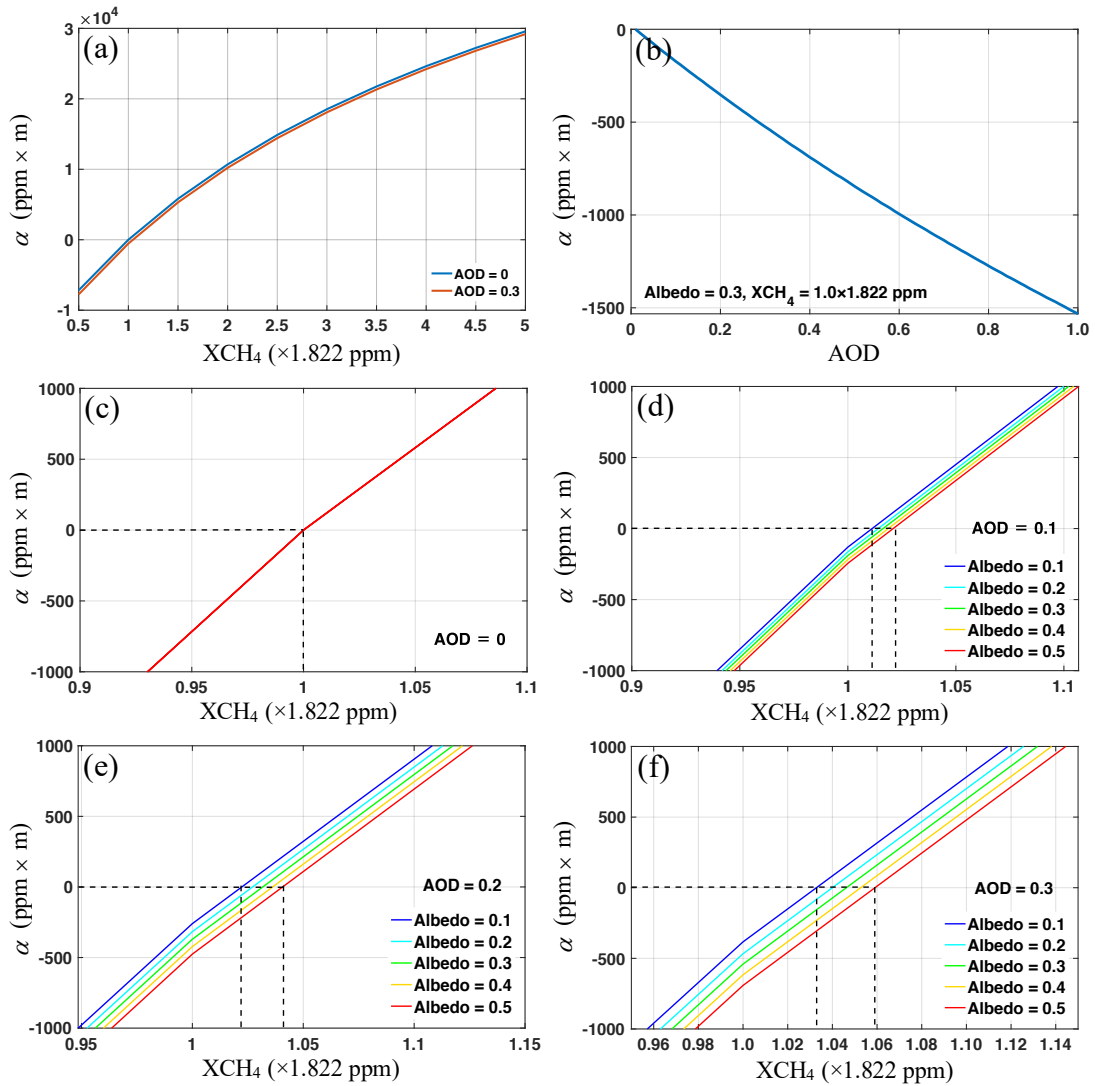


756

757 **Figure 4: Retrieval image for the plume center (500 elements) based on the (a) MF method and (b) OE method.**

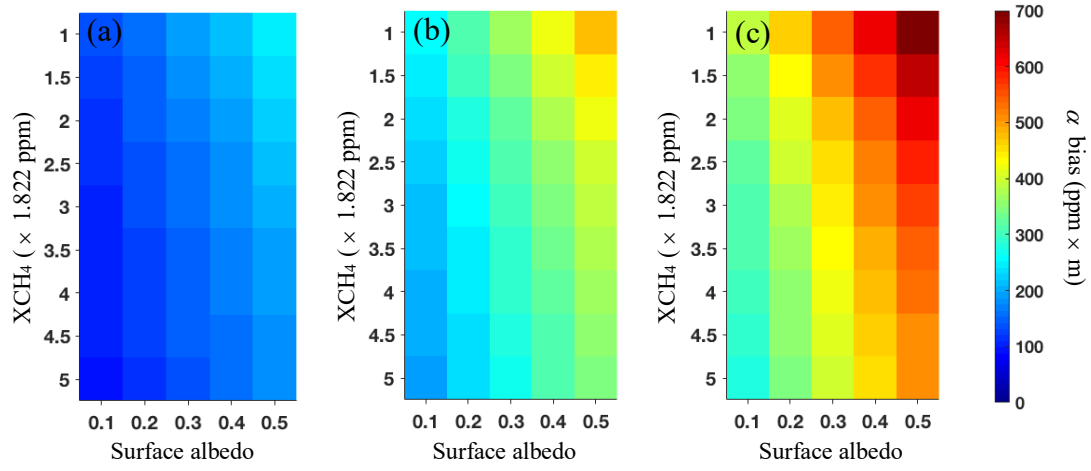
758

759
760



761 Figure 5: (a) α as a function of XCH_4 for AOD = 0 and AOD = 0.3 (surface albedo = 0.3). (b) α as a function
762 of AOD ($XCH_4 = 1.0 \times 1.822$ ppm, surface albedo = 0.3). Zoomed in versions of α as a function of XCH_4 for
763 different surface albedos (0.1-0.5), where (c) AOD = 0, (d) AOD = 0.1, (e) AOD = 0.2, and (f) AOD = 0.3.
764

765



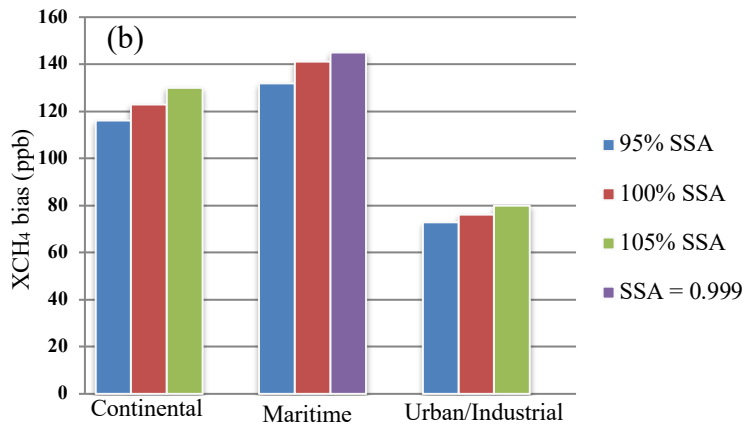
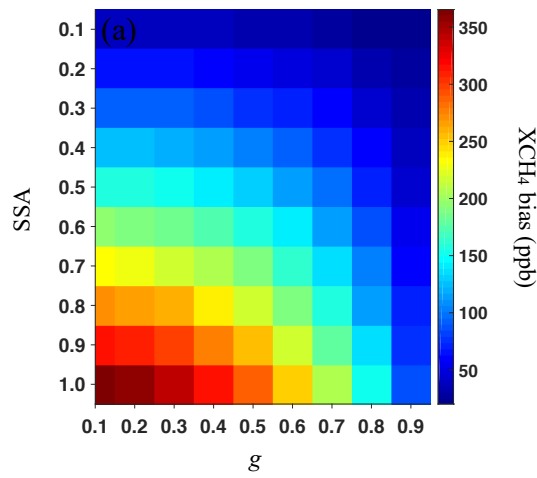
766

767 **Figure 6: Bias in α as a function of XCH₄ and surface albedo for (a) AOD = 0.1, (b) AOD = 0.2, and (c) AOD**
768 **= 0.3.**

769

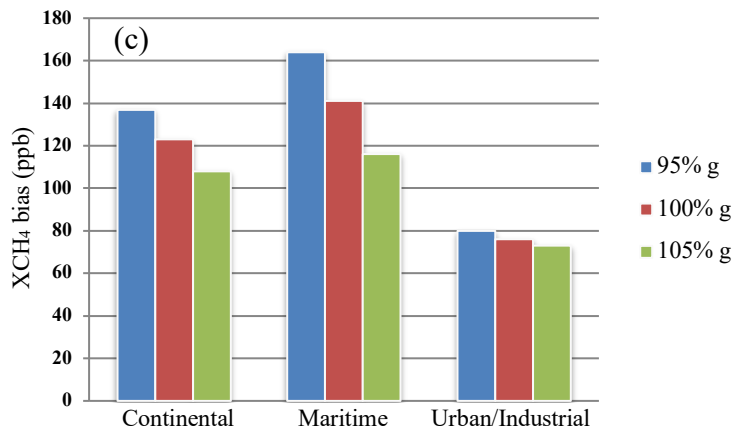
770

771



772

773



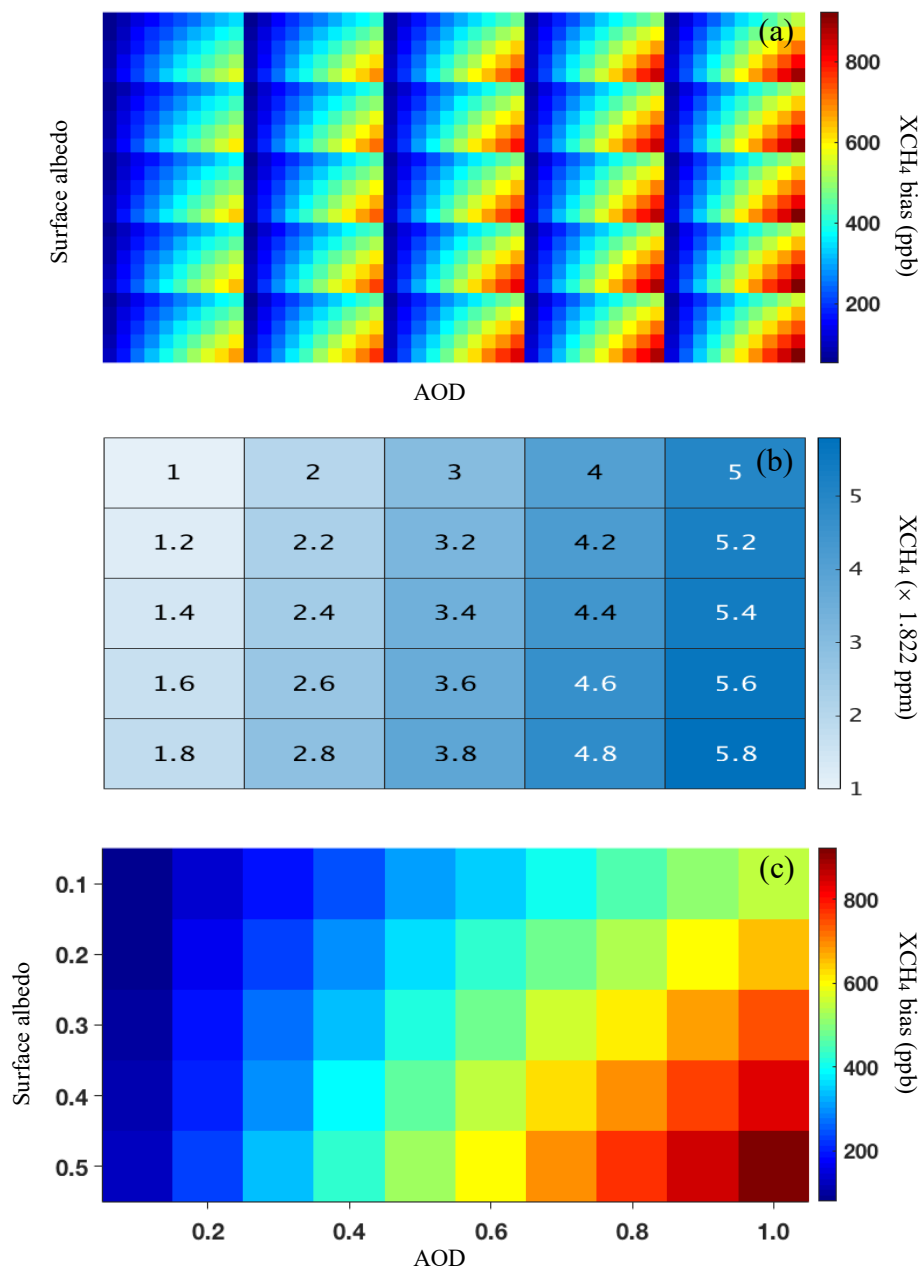
774

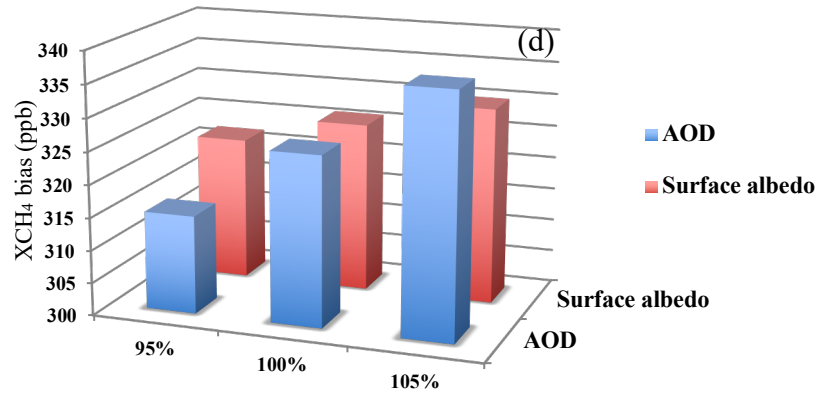
775

776

777

Figure 7: (a) CH₄ retrieval biases for different values of g and SSA. Surface albedo, AOD = 0.3, XCH₄ = 1.0 × 1.822 ppm. (b) CH₄ retrieval biases for a ± 5% change in SSA for the three aerosol mixture models. (c) Same as (b), but for a ± 5% change in g .





780

781 **Figure 8: (a) CH₄ retrieval biases for different values of XCH₄, AOD and surface albedo. $g = 0.75$, $SSA = 0.95$.**

782 **(b) XCH₄ for each box in (a). (c) Zoomed in plot of bottom right box (XCH₄ = 5.8×1.822 ppm). The x and y**

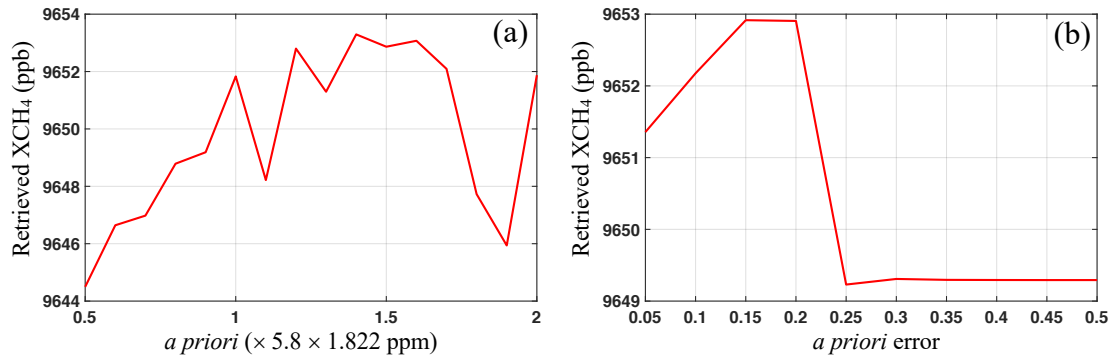
783 **axes show the variation of AOD and surface albedo, respectively. These changes are identical for every box**

784 **in (a). (d) CH₄ retrieval biases for a $\pm 5\%$ change in AOD and surface albedo from a base value of 0.3 ($g =$**

785 **0.75 , $SSA = 0.95$, XCH₄ = 5.8×1.822 ppm).**

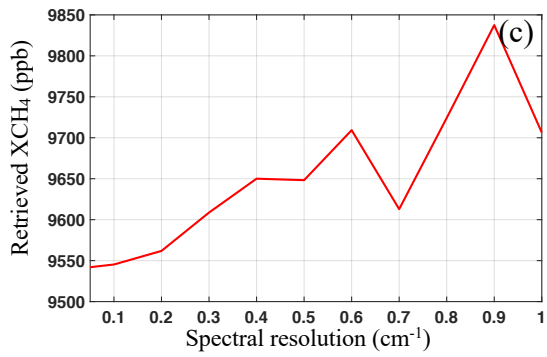
786

787



788

789

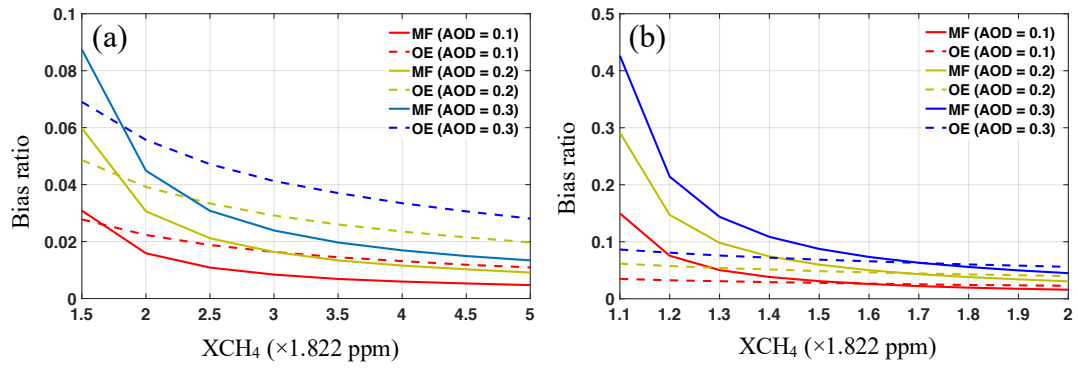


790

791 **Figure 9: Retrieved XCH₄ for different values of (a) *a priori* (*a priori* error = 0.2), (b) *a priori* error (*a priori* =**
792 **5.5 × 1.822 ppm) and (c) spectral resolution. *g* = 0.75, SSA = 0.95, AOD = 1.0, surface albedo = 0.5, XCH₄ =**
793 **5.8 × 1.822 ppm.**

794

795



796 **Figure 10: (a) Bias ratio as a function of CH₄ concentration for the two retrieval techniques, where the XCH₄**
797 **ranges from 1.5 to 5 ($\times 1.822$ ppm). (b) Same as (a), but for XCH₄ ranging from 1.1 to 2 ($\times 1.822$ ppm). Surface**
798 **albedo is set to 0.3 for all cases; results for the MF and OE methods are shown by solid and dashed lines,**
799 **respectively.**
800

801

	Dust-like	Water soluble	Oceanic	Soot
SSA	0.805	0.799	0.970	0.014
<i>g</i>	0.926	0.550	0.816	0.092

802 **Table 1: Optical properties of basic aerosol types (WCRP, 1986).**

803

		Continental	Maritime	Urban/Industrial
Aerosol component	Dust-like	70%		17%
	Water soluble	29%	5%	61%
	Oceanic		95%	
	Soot	1%		22%
SSA		0.746	0.966	0.314
<i>g</i>		0.764	0.810	0.586

804 **Table 2: Optical properties of three aerosol mixture models (WCRP, 1986).**

805

806

Attribute	Values
Sensor height	1 km
View zenith angle	11.91°
Solar zenith angle	30.75°
Relative azimuth angle	22.87°
Aerosol loading region	surface to 1 km
SSA	0.95
<i>g</i>	0.75

807 **Table 3: Inputs for the 2S-ESS model simulation.**

808